Title

AuPb$_2$I$_7$: A Narrow Bandgap Au^{3+} Iodide Semiconductor

Journal

Inorganic Chemistry, 57(2)

ISSN

0020-1669 1520-510X

Authors

Alexander, Grant C. B
Fabini, Douglas H
Seshadri, Ram
et al.

Publication Date

2018-01-02

DOI

10.1021/acs.inorgchem.7b02723

Peer reviewed

$AuPb_2I_7$: A Narrow Bandgap Au^{3+} Iodide Semiconductor

Grant C. B. Alexander[1], Douglas H. Fabini[2,3], Ram Seshadri[2,3,4], and Mercouri G. Kanatzidis [1,*]

[1] *Department of Chemistry, Northwestern University, Evanston, Illinois 60208, United States*

[2] *Materials Research Laboratory,* [3] *Materials Department, and* [4] *Department of Chemistry and Biochemistry, University of California, Santa Barbara, California 93106, USA*

Abstract

The unusual Au^{3+} ternary halide $AuPb_2I_7$ has been isolated from reactions of AuI, PbI_2, and I_2. $AuPb_2I_7$ crystallizes in the triclinic *P*-1 space group as micron-scale needles with cell dimensions a = 4.5170(3) Å, b = 7.3847(4) Å, c = 12.2970(7) Å, α = 76.374(4)°, β = 83.711(4)°, γ = 72.987(3)° at room temperature with ρ = 6.538 g/cm^3 and has no structural phase transition down to 100 K. The title compound has a unique three-dimensional structure composed of $[Pb_2I_7]^{3-}$ pseudo-layers extending in [010] bridged by square planar Au^{3+} at an oblique angle in the [001] direction. The pseudo-layers are composed of $^1/_\infty[Pb_2I_2]^{2+}$ chains propagating down [100] linked by square planar I^- ions through [010]. $AuPb_2I_7$ has a band gap of 1.17 eV and is stable in air for a several days, before degrading to PbI_2, Au^0, and I_2. Density Functional Theory calculations show that $AuPb_2I_7$ is an indirect bandgap semiconductor where the band gap stems predominantly from Au – I metal ligand charge transfer.

Introduction

The class of heavy-metal halide semiconductors without organic cations has sparked a quickly growing interest in understanding their structural chemistry and optoelectronic properties for potential uses in various electronic devices including hard and soft radiation detection.[1-5] In particular, there is a search for alternative materials to alleviate the stability issues which plague the organic-inorganic hybrid perovskites.[6] Such efforts have focused on alternative B-site cations for the AMX_3 perovskites[1, 7], perovskite-like phases[8-9], and the $A_3M'_2X_9$ defect perovskite phases where A = Rb, Cs, Tl; M = Pb; M' = Bi, Sb; X = I, Br, Cl.[5, 10] Very little perovskite chemistry has been reported when the A site is not an alkali ion but a group 11 ion. Literature reveals that no report of $CuPbI_3$, and the $AgI - PbI_2$ system is shown only to have ordered mixtures at elevated temperatures.[11] Thus, Au remains the last system to investigate.

In the case of ternary Au halides, few have been isolated as purely inorganic phases[12-14], and even fewer with iodine as a direct ligand to Au.[14-17] First are the monoclinic phases of an alkali metal ion with Au in the 3+ oxidation state, such as $LiAuI_4$ and $KAuI_4$, having molecular square planar $[AuI_4]^-$ units charge balanced by the alkali metal cation, Figure 1a. Rb and Cs stabilize the formation of tetragonal perovskite-like $Rb_2[AuI_4][AuI_2]$ and $Cs_2[AuI_4][Au^{I}I_2]$, Figure 1b.[15, 17] In these phases gold is found in two different valence states (1+ and 3+), alternating in square planar and linear coordination to form the pseudo-perovskite lattice encapsulating the cation. There are no current reports of Au being substituted on the A site of AMI_3 phases. Au^{1+} is much smaller than Rb or Cs, and if it could be incorporated it would surely destabilize the perovskite-type lattice but it could be expected to form other structure types similar to $TlPbI_3$ which is two dimensional.[18]

Here were report that our attempts to produce "$AuPbI_3$" led to the isolation of the surprising compound $AuPb_2I_7$ which does not contain Au^+ but is composed of anisotropic pseudo-layers of a 3D structure of extended $[Pb_2I_7]^{3-}$ pseudo-layers bridged by square planar Au^{3+}. $AuPb_2I_7$ is the first reported gold heavy metal halide to be structurally characterized. $AuPb_2I_7$ grows on the surface of recrystallized PbI_2 from the off-stoichiometric reactions of AuI and PbI_2 as well as direct synthetic methods with I_2. The compound is black with an experimental band gap of 1.17 eV. Density Functional Theory calculations demonstrate an indirect bandgap semiconductor.

EXPERIMENTAL SECTION

Synthesis

All chemicals were used as obtained from the supplier: AuI, PbI_2, and I_2 (99.999%, Sigma-Aldrich, St. Louis, MO). 1 to 1 and 1 to 2 ratios of AuI and PbI_2 were used for initial off stoichiometry syntheses at the 1 mmol (323.8 mg AuI and 461.0 or 921.0 mg PbI_2) or 2 mmol (627.6 mg AuI and 921 mg or 1842 mg PbI_2). For direct syntheses 1 mmol scale stoichiometric ratios of AuI (323.8 mg), PbI_2 (921 mg), and I_2 (253.8 mg) were used. All materials were weighed, mixed, and transferred into 13 mm fused quartz tubes on the benchtop. Tubes were sealed at or below 3×10^{-3} mbar and heated to 600 C in 48 hours, held for 48 hours, and cooled to 30 C in 24 hours. Minute quantities of micron-scale black crystals of the title compound grow on surfaces of recrystallized PbI_2. Due to crystallization on the surface of PbI_2, $AuPb_2I_7$ proves difficult to mechanically isolate as a pure phase (Yield: 0.1g, Less than 10% based on Au).

A vapor transport experiment was also conducted; 1 mmol AuI (323.8 mg), 2 mmol of PbI_2 (921 mg), and 1.2 mmol of I_2 (304.6 mg) were combined on the bench and sealed in a fused quartz tube at or below 3×10^{-3} mbar. A slight excess of I_2 was added to help function as a transport agent.

The tube measured approximately 230 mm, and was centered in a horizontal two zone furnace with the hot zone set to 450 C and cold zone set to 200 C. Reagents were set in the hot zone. For both zones temperature controllers were set to ramp to the target temperature in 10 hours, hold for 72 hours, and cool to room temperature in 15 hours. No transport of the title compound was achieved, but unreacted PbI_2 was transported away from the product yielding slightly easier isolation. Micron scale crystals can be isolated in small quantities for optical and single crystal diffraction experiments (Yield: 0.1g, Less than 10% based on Au).

Single Crystal X-Ray Diffraction

Single Crystals of $AuPb_2I_7$ were isolated from the reaction mixture under Paratone N oil to shield samples from oxygen. Samples of sufficient size were isolated off the surface of PbI_2 for X-ray diffraction. Once selected the small needles were mounted on a MiTeGen™ mounts using Paratone N oil. Diffraction was conducted at 298 K and 100 K on a Bruker KAPPA APEX diffractometer with a MoKα microsource and Quazar™ optics monochromator. Using the COSMO program provided in the APEX 3 software, data collection strategy with a series of 0.5° scans in ω and φ was determined.[19] The exposure time was 10 s/frame, and the crystal-to-detector distance was 60 mm. SADABS or TWINABS was used for face-indexed absorption, incident beam, and decay corrections.[20-21] The structure solved by the direct method and refined on F^2 using the SHELX14 program suite.[22] All atoms were refined anisotropically.

Powder X-ray diffraction

The presence of $AuPb_2I_7$ was verified by power diffraction using a Rigaku Miniflex power X-ray diffractometer with Ni-filtered Cu Kα radiation operating at 30 kV and 15 mA. Scans were

performed with a resolution of 0.02° and a scan rate of 10°/min. Simulated powder patterns of $AuPb_2I_7$ were calculated using the refined room-temperature crystal structure CIF with MERCURY, part of the CSD software suite.[23]

Scanning Electron Microscopy

A Hitachi S-3400 scanning electron microscope equipped with a PGT energy-dispersive X-ray analyzer was used to acquire images and semi quantitative EDS analyses. Spectra were collected using an accelerating voltage of 25 KeV and current of 70 uA for 60 s. No reduction of Au was observed during the SEM experiments due to the electron beam. The reported composition from EDS is based on multiple independent spectra, see supporting information.

Solid State UV-Vis Spectroscopy

A Shimadzu UV-3600 PC double-beam, double-monochromator spectrophotometer was used to collect diffuse-reflectance spectra in the range of 200−2500 nm. The instrument was equipped with an integrating sphere and controlled by a personal computer. $BaSO_4$ was used as a standard and set to 100% reflectance. Samples were prepared by quickly placing the ground crystalline products on a bed of BaSO4 in air. Collected reflectance data were converted to absorbance according to the Kubelka−Munk equation $\alpha/S = (1 - R)2 /2R$, where α is the absorption coefficient, S is the scattering coefficient, and R is the reflectance.[24] The band gap was determined by extrapolating the intercept of the fitted converted data.

Density Functional Theory (DFT) Calculations

Calculations of the electronic structure were performed with the Vienna Ab initio Simulation Package (VASP)[25-28] which implements the Kohn–Sham formulation of density functional theory (DFT) using a plane wave basis set and the projector augmented wave formalism.[29-30] The generalized gradient approximation was employed using the exchange and correlation functional of Perdew, Burke, and Ernzerhof (GGA–PBE), with and without the inclusion of spin-orbit coupling (SOC).[31] Hybrid functional calculations which incorporate exact exchange were prohibitively expensive due to the low symmetry and heavy atoms. Electrons were included in the valence as follows: Au, $6s^2 5d^9$; Pb, $6s^2 5d^{10} 6p^2$; I, $5s^2 5p^5$. The plane wave basis set cutoff energy (500 eV) and k-point mesh density (9×5×3 for total energy and band calculations, 15×9×5 for density of states, all Monkhorst–Pack sampling[32]) were chosen based on convergence of the total energy. The Brillouin zone path for band structure calculations was taken from Setyawan and Curtarolo.[33] Ground-state DFT structure relaxations poorly reproduced the experimental structures, in a manner similar to other soft metal halides. However, unlike higher symmetry crystals (where the differences between DFT and experiment are more isotropic), the highly anisotropic connectivity of $AuPb_2I_7$ leads to significant shearing of the unit cell (such that the lattice angle α becomes more acute). As such, the experimental crystal structure was employed for electronic structure calculations. The net forces on the ions in the experimental structure were highest for the iodine labeled "I1" in Table 2.

RESULTS AND DISCUSSION

Synthesis

All reactions performed between AuI and PbI_2 aimed at obtaining a $AuPbI_3$ or $AuPb_2I_5$ compositions failed to do so. No evidence for the existence of such phases was present, however,

we were able to obtain black needle-like crystals of the ternary compound $AuPb_2I_7$. Despite many attempts at synthesizing a pure phase of $AuPb_2I_7$, the compound grows directly on the surface of PbI_2 crystals, Figure 2, and forms regardless of the ratio of AuI and PbI_2 combined. To balance charge in this phase, the Au must be in the 3+ oxidation state. Because the starting Au source is AuI, to form $AuPb_2I_7$ Au^I must undergo the oxidation *in situ* to Au^{3+}. However, this oxidation must be a disproportionation reaction of Au^+ to Au^0 and Au^{3+}, and therefore removes gold metal from the reaction, which can be observed in Figure 3.

To mitigate Au loss to disproportionation, iodine was added to the reaction mixture to act as an oxidant. The direct method of synthesis with I_2 yields slightly more product, but the reaction products remain a mixture of $AuPb_2I_7$, PbI_2, I_2, and Au^0, Figure 3. Varying the reaction heating rate, soak time, and cooling rate from 6 to 48 hours did not show any significant effect on the formation fraction of $AuPb_2I_7$. Attempting vapor transport did not yield significant improvement in isolating the $AuPb_2I_7$, however due to the temperature gradient, PbI_2 was transported away from the product, localizing most of the growth of the title compound on the non-transported PbI_2. This can be seen in the larger patches of growth, but underneath remains the PbI_2 substrate, Figure 4a. $AuPb_2I_7$ decomposes slowly in air to yield Au^0, PbI_2 and I_2, which is unsurprising as the previously discussed Au iodide compounds all undergo the same reduction. This is evident in Figure 4b, where Au has physically expelled itself from the crystal matrix.

Crystal Structure Description

$AuPb_2I_7$ crystallizes in the triclinic *P*-1 space group (No. 2) and presents a 3D structure of extended $[Pb_2I_7]^{3-}$ pseudo-layers extending in [010] bridged by square planar Au^{3+} at an oblique

angle in the [001] direction. See Tables 1 – 4 for crystallographic data pertaining to refinement details, atom coordinates, anisotropic parameters, and selected bond distances and angles. The $[Pb_2I_7]^{3-}$ layers can be better described as $^1/_\infty[Pb_2I_2]^{2+}$ backbone-like chains propagating down [100] linked by square planar I^- along [010], Figure 5. A full view of the ball and stick representation of the structure is shown in Figure 6. The Au atom must be 3+ to charge balance the stoichiometry.

Au^{3+} sits in a square planar site bridging the layers together such that a three-dimensional structure is attained. The plane of the $[AuI_4]^-$ unit does not correspond to any cardinal coordinate, and is oblique to [001]. Bond distances for the $[AuI_4]^-$ are within 2.6330(9) to 2.6344(9) Å, which agrees with other square planar Au^{3+} in $A_2Au^IAu^{III}I_6$ compounds that report 2.644 Å or 2.645 Å for A = Rb, Cs respectively, Figure 7.[8, 10]

The Pb^{2+} atom is eight coordinate, Figure 8a,b, and forms distorted hendecahedra that are face-sharing in the [001] direction and edges at an angle oblique to [010] to other Pb hendecahedrons, Figure 8c. When $[AuI_4]^-$ and square planar I^- are considered discrete units, this suggests the $^1/_\infty[Pb_2I_2]^{2+}$ backbone that propagates down [100], Figure 8c. The 8 Pb – I bonds range from 3.1149(10) to 3.8247(12) Å, figure 8b. Seven of the eight bonds agree with the hendecahedral bonds seen in $InPb_2I_5$ where they range from 3.123 to 3.573 Å.[34] The final coordination of Pb to I in the hendecahedra extends to 3.8247(12) Å, which is unprecedentedly long and occurs due to the stereo active lone pair that resides on the Pb atom, which pushes the I atom further away from the coordination sphere.

Within the structure, the iodine atoms occupy four sites and exhibit three different coordination environments. First, two iodine atoms act as a both part of the hendecahedral geometry of Pb and the square planar geometry of Au which can readily be observed in Figure 6. They coordinate in a distorted half trigonal prismatic geometry between two Pb atoms and Au,

with the longest 'bond' being 3.8247(12) Å for the distant Pb. The $^{1}/_{\infty}[Pb_2I_2]^{2+}$ backbone contains another distorted half trigonal prismatic coordinated iodine between three Pb atoms mimicking the coordination in PbI_2 in the [100] direction, Figure 8c. The final iodine sits in a unique square planar geometry between 4 Pb atoms and links the $^{1}/_{\infty}[Pb_2I_2]^{2+}$ backbones together to form the pseudo-layered structure, Figure 8d.

The overarching structure of $AuPb_2I_7$ does not undergo a phase transition at low temperature with lattice parameters shrinking predictably. However, at 100 K the $[AuI_4]^-$ unit distorts and Au – I bonds elongate and shorten from 2.6340(11) and 2.6328(10) Å to 2.7986(15) and 2.5464(12) Å respectively. Additional bond shortening in the Pb hendecahedron allows the unit cell to be drawn differently, figure S5, due to the reduction in the distance between square planar iodide atoms from 12.7657(8) to 12.226(3) Å. Further details of the low temperature structure are given in the supplementary information.

Optical Absorption and Electronic Structure

The band gap of black $AuPb_2I_7$ was determined to be 1.17 eV by UV-vis diffuse reflectance spectroscopy measurements, Figure 9. Here optical absorption is dominated by metal-ligand charge transfer transitions within the $[AuI_4]^-$ unit, thus acting as strong chromophore. This interpretation is supported by the DFT calculations below.

The calculated electronic band structure and density of states (DOS) for $AuPb_2I_7$ (Figure 10) indicates a small bandgap (0.35 eV) between valence bands derived primarily from I *p* orbitals and a single conduction band derived primarily from an empty Au *d* orbital, consistent with a square planar crystal field for d^8 Au^{3+}. Relatively weak mixing of the filled Pb *s* states with the iodine orbitals (due to the distorted hendecahedral coordination) leads to rather localized, slightly

bonding Pb *s* states nearly 8 eV below the Fermi level, and weak, slightly antibonding Pb *s* contributions to the valence bands within ~2 eV of the Fermi level. The unoccupied Pb *p* states are substantially higher in energy than the lowest conduction band, and are unlikely to be responsible for optical absorption near the absorption onset. The magnitude of the underestimate of the observed bandgap is typical of calculations employing the generalized gradient approximation. Spin-orbit coupling has a significant impact only on the higher-lying excited states derived from Pb *p* orbitals (Supporting Information, Figure S2).

The calculated bandgap is indirect, between the valence band maximum along R–Γ and the conduction band minimum at R. Given the narrow bandwidths, there are multiple local extrema within a few 10s of meV of the band edges, and the details of the electronic structure may change with a more sophisticated treatment of exchange and correlation. The effective masses of holes and electrons along the R–Γ direction are calculated as $1.3m_e$ and $2.3m_e$, respectively. Wavevectors near the band edges correspond to traveling waves at a slightly oblique angle to the pseudo-layers that stack along [010], suggesting the bridging iodine atoms participate in charge transport. Thus, despite the rather heavy carriers, the material is best thought of as 3D in an electronic sense, rather than layered. This is consistent with the absence of obvious excitonic features in the optical absorption, in contrast to layered halides with significant dielectric confinement and correspondingly large exciton binding energies.[35]

CONCLUSION

Here we reported the synthesis and subsequent characterization of the novel Au^{3+} semiconductor $AuPb_2I_7$. The structure presents the modification of the PbI_2 sublattice, causing the formation of a three-dimensional anisotropic network of $1/\infty[Pb_2I_2]^{2+}$ chains bridged by $[AuI_4]^-$

and square planar I^-. The experimental band gap was found to be approximately 1.17 eV. Ab initio calculations indicate the lowest energy excited states derive from the empty *d* orbital of the square planar d^8 Au^{III}. $AuPb_2I_7$ demonstrates the versatility of the PbI_2 lattice to incorporate Au^{3+} and suggests that further investigation of lattice modifications in PbI_2, as new interesting structures are surely undiscovered.

SUPPORTING INFORMATION

Supporting information is available and contains: SEM-EDS results, powder diffraction patterns of different syntheses, photo of vapor transport product, additional crystallographic parameters for low temperature data, band structure diagram.

ACKNOWLEDGEMENTS

Work was supported by the U.S. Department of Energy, Office of Science (Grant No. SC0012541). This work made use of the X-Ray facilities in IMSERC at Northwestern University, which has received support from the Soft and Hybrid Nanotechnology Experimental (SHyNE) Resource (NSF NNCI-1542205); the State of Illinois and International Institute for Nanotechnology (IIN). The SEM/EDS work was performed in the EPIC facility of the NUANCE Center at Northwestern University. DHF thanks the National Science Foundation Graduate Research Fellowship Program for support under Grant DGE 1144085. We acknowledge support from the Center for Scientific Computing from the CNSI, MRL: an NSF MRSEC (DMR-1121053) and NSF CNS-0960316.

REFERNECE

1. Stoumpos, C. C.; Malliakas, C. D.; Peters, J. A.; Liu, Z.; Sebastian, M.; Im, J.; Chasapis, T. C.; Wibowo, A. C.; Chung, D. Y.; Freeman, A. J.; Wessels, B. W.; Kanatzidis, M. G., Crystal Growth of the Perovskite Semiconductor CsPbBr3: A New Material for High-Energy Radiation Detection. *Cryst. Growth Des.* **2013,** *13*, 2722-2727.
2. Saparov, B.; Hong, F.; Sun, J.-P.; Duan, H.-S.; Meng, W.; Cameron, S.; Hill, I. G.; Yan, Y.; Mitzi, D. B., Thin-Film Preparation and Characterization of Cs3Sb2I9: A Lead-Free Layered Perovskite Semiconductor. *Chem. Mater.* **2015,** *27*, 5622-5632.
3. Stoumpos, C. C.; Kanatzidis, M. G., The Renaissance of Halide Perovskites and Their Evolution as Emerging Semiconductors. *Acc. Chem. Res.* **2015,** *48*, 2791-2802.
4. Hu, Y.; Zhang, S.; Miao, X.; Su, L.; Bai, F.; Qiu, T.; Liu, J.; Yuan, G., Ultrathin Cs3Bi2I9 Nanosheets as an Electronic Memory Material for Flexible Memristors. *Adv. Mater. Interfaces* **2017,** *4*, 1700131-n/a.
5. McCall, K. M.; Stoumpos, C. C.; Kostina, S. S.; Kanatzidis, M. G.; Wessels, B. W., Strong Electron–Phonon Coupling and Self-Trapped Excitons in the Defect Halide Perovskites A3M2I9 (A = Cs, Rb; M = Bi, Sb). *Chem. Mater.* **2017,** *29*, 4129-4145.
6. Niu, G.; Guo, X.; Wang, L., Review of recent progress in chemical stability of perovskite solar cells. *J. Mater. Chem. A* **2015,** *3*, 8970-8980.
7. Stoumpos, C. C.; Frazer, L.; Clark, D. J.; Kim, Y. S.; Rhim, S. H.; Freeman, A. J.; Ketterson, J. B.; Jang, J. I.; Kanatzidis, M. G., Hybrid Germanium Iodide Perovskite Semiconductors: Active Lone Pairs, Structural Distortions, Direct and Indirect Energy Gaps, and Strong Nonlinear Optical Properties. *J. Am. Chem. Soc.* **2015,** *137*, 6804-6819.
8. Lin, W.; Stoumpos, C. C.; Liu, Z.; Das, S.; Kontsevoi, O. Y.; He, Y.; Malliakas, C. D.; Chen, H.; Wessels, B. W.; Kanatzidis, M. G., TlSn2I5, a Robust Halide Antiperovskite Semiconductor for γ-Ray Detection at Room Temperature. *ACS Photonics* **2017,** *4*, 1805-1813.
9. Qiu, X.; Cao, B.; Yuan, S.; Chen, X.; Qiu, Z.; Jiang, Y.; Ye, Q.; Wang, H.; Zeng, H.; Liu, J.; Kanatzidis, M. G., From unstable CsSnI3 to air-stable Cs2SnI6: A lead-free perovskite solar cell light absorber with bandgap of 1.48 eV and high absorption coefficient. *Sol. Energy Mater. Sol. Cells* **2017,** *159*, 227-234.
10. Lehner, A. J.; Fabini, D. H.; Evans, H. A.; Hébert, C.-A.; Smock, S. R.; Hu, J.; Wang, H.; Zwanziger, J. W.; Chabinyc, M. L.; Seshadri, R., Crystal and Electronic Structures of Complex Bismuth Iodides A3Bi2I9 (A = K, Rb, Cs) Related to Perovskite: Aiding the Rational Design of Photovoltaics. *Chem. Mater.* **2015,** *27*, 7137-7148.
11. Brightwell, J. W.; Buckley, C. N.; Ray, B., Electrical and phase behaviour of the system AgI-PbI2. *Solid State Commun.* **1982,** *42*, 715-716.
12. Strähle, J.; Bärnighausen, H., Kristallchemischer Vergleich der Strukturen von RbAuCl4 und RbAuBr4. *Z. Kristallogr* **1971,** *134*, 471.
13. Eijndhoven, J. C. M. T.-v.; Verschoor, G. C., Redetermination of the crystal structure of Cs2AuAuCl6. *Mater. Res. Bull.* **1974,** *9*, 1667-1670.
14. Strähle, J.; Gelinek, J.; Kölmel, M.; Nemecek, A.-M., Die Kristallstruktur der Salze K2Au2I6 und Cs2AgxAuI1-xAuIIIBr6. Ein Beitrag zur Kristallchemie der Alkalihexahalogenoaurate(I,III) / Crystal Structure of the Salts K2Au2I6 and Cs2AgxAuI1-xAuIIIBr6. A Contribution to the Crystal Chemistry of the Alkali Hexahalogeno Aurates(I,III). In *Z. Naturforsch., B: J. Chem. Sci.*, **1979**, 34, 1047.

15. Matsushita, N.; Kitagawa, H.; Kojima, N., A Three-Dimensional Iodo-Bridged Mixed-Valence Gold(I, III) Compound, Cs2AuIAuIIII6. *Acta Crystallogr., Sect. C: Struct. Chem.* **1997,** *53*, 663-666.
16. Schulz Lang, E.; Abram, U.; Strähle, J., Synthese, Eigenschaften und Struktur von LiAuI4 und KAuI4 mit einer Diskussion der kristallchemischen Verwandtschaft zwischen den Halogenoauraten RbAuCl4, AgAuCl4, RbAuBr4 und LiAuI4. *Z. Anorg. Allg. Chem.* **1997,** *623*, 1791-1795.
17. Matsushita, N.; Tanaka, A.; Kojima, N., A three-dimensional iodo-bridged mixed-valence gold(I,III) compound, Rb2[AuII2][AuIIII4]. *Acta Crystallogr., Sect. E: Struct. Rep. Online* **2005,** *61*, i201-i203.
18. Khyzhun, O.; Fochuk, P.; Kityk, I.; Piasecki, M.; Levkovets, S.; Fedorchuk, A.; Parasyuk, O., Single crystal growth and electronic structure of TlPbI 3. *Mater. Chem. Phys.* **2016,** *172*, 165-172.
19. Bruker-AXS, APEX3 (version 2016.1-0) **2016**, Madison, WI, 2016.
20. Krause, L.; Herbst-Irmer, R.; Sheldrick, G. M.; Stalke, D., Comparison of silver and molybdenum microfocus X-ray sources for single-crystal structure determination. *J. Appl. Crystallogr.* **2015,** *48*, 3-10.
21. Sheldrick, G. M. *TWINABS*, University of Göttingen, Germany., 2012.
22. Sheldrick, G. M., Crystal structure refinement with SHELXL. *Acta Crystallogr., Sect. C: Struct. Chem.* **2015,** *71*, 3-8.
23. Macrae, C. F.; Edgington, P. R.; McCabe, P.; Pidcock, E.; Shields, G. P.; Taylor, R.; Towler, M.; Streek, J. v. d., Mercury: visualization and analysis of crystal structures. *J. Appl. Crystallogr.* **2006,** *39*, 453-457.
24. Kortüm, G.; Braun, W.; Herzog, G., Prinzip und Meßmethodik der diffusen Reflexionsspektroskopie. *Angew. Chem.* **1963,** *75*, 653-661.
25. Kresse, G.; Hafner, J., Ab initio. *Phys. Rev. B: Condens. Matter* **1993,** *47*, 558-561.
26. Kresse, G.; Hafner, J., Ab initio. *Phys. Rev. B: Condens. Matter* **1994,** *49*, 14251-14269.
27. Kresse, G.; Furthmüller, J., Efficient iterative schemes for ab initio total-energy calculations using a plane-wave basis set. *Phys. Rev. B: Condens. Matter* **1996,** *54*, 11169-11186.
28. Kresse, G.; Furthmüller, J., Efficiency of ab-initio total energy calculations for metals and semiconductors using a plane-wave basis set. *Comput. Mater. Sci.* **1996,** *6*, 15-50.
29. Blöchl, P. E., Projector augmented-wave method. *Phys. Rev. B: Condens. Matter* **1994,** *50*, 17953-17979.
30. Kresse, G.; Joubert, D., From ultrasoft pseudopotentials to the projector augmented-wave method. *Phys. Rev. B: Condens. Matter* **1999,** *59*, 1758-1775.
31. Perdew, J. P.; Burke, K.; Ernzerhof, M., Generalized Gradient Approximation Made Simple. *Phys. Rev. Lett.* **1996,** *77*, 3865-3868.
32. Monkhorst, H. J.; Pack, J. D., Special points for Brillouin-zone integrations. *Phys. Rev. B: Condens. Matter* **1976,** *13*, 5188-5192.
33. Setyawan, W.; Curtarolo, S., High-throughput electronic band structure calculations: Challenges and tools. *Comput. Mater. Sci.* **2010,** *49*, 299-312.
34. Becker, D.; Beck, H. P., High Pressure Study of NH4Pb2Br5 Type Compounds. I structural parameters and their evolution under high pressure. *Z. Anorg. Allg. Chem.* **2004,** *630*, 1924-1932.
35. Cao, D. H.; Stoumpos, C. C.; Farha, O. K.; Hupp, J. T.; Kanatzidis, M. G., 2D Homologous Perovskites as Light-Absorbing Materials for Solar Cell Applications. *J. Am. Chem. Soc.* **2015,** *137*, 7843-7850.

Table 1. Crystal data and structure refinement for $AuPb_2I_7$ at 100 and 298 K.

Formula weight	1499.65	1499.65
Temperature	100 K	298 K
Wavelength	0.71073 Å	0.71073 Å
Crystal system	Triclinic	Triclinic
Space group	*P*-1	*P*-1
Unit cell dimensions	a = 4.4803(9) Å, α = 76.29(3)° b = 7.3443(15) Å, β = 84.00(3)° c = 12.226(3) Å, γ = 73.06(3)°	a = 4.5170(3) Å, α = 76.374(4)° b = 7.3847(4) Å, β = 83.711(4)° c = 12.2970(7) Å, γ = 72.987(3)°
Volume	373.60(15) $Å^3$	380.83(4) $Å^3$
Z	1	1
Density (calculated)	6.665 g/cm^3	6.539 g/cm^3
Absorption coefficient	46.683 mm^{-1}	45.797 mm^{-1}
F(000)	614	614
Crystal size	0.129 x 0.041 x 0.02 mm^3	0.027 x 0.042 x 0.067 mm^3
θ range for data collection	1.716 to 24.999°	1.706 to 24.999°
Index ranges	-5<=h<=5, -8<=k<=8, 0<=l<=14	-5<=h<=5, -8<=k<=8, -14<=l<=14
Reflections collected	5840	6032
Independent reflections	1279 [R_{int} = 0.0363]	1346 [R_{int} = 0.0437]
Completeness to θ = 26.000°	97.8%	99.8%
Refinement method	Full-matrix least-squares on F^2	Full-matrix least-squares on F^2
Data / restraints / parameters	1279 / 0 / 50	1346 / 0 / 49
Goodness-of-fit	1.235	1.067
Final R indices [I > 2σ(I)]	R_{obs} = 0.0365, wR_{obs} = 0.1201	R_{obs} = 0.0335, wR_{obs} = 0.0804
R indices [all data]	R_{all} = 0.0376, wR_{all} = 0.1235	R_{all} = 0.0406, wR_{all} = 0.0880
Largest diff. peak and hole	2.848 and -3.664 $e \cdot Å^{-3}$	2.929 and -1.602 $e \cdot Å^{-3}$

$R = \Sigma||F_o|-|F_c|| / \Sigma|F_o|$, $wR = (\Sigma[w(|F_o|^2 - |F_c|^2)^2] / \Sigma[w(|F_o|^4)])^{1/2}$ and $w=1/[\sigma^2(Fo^2)+(0.0155P)^2+4.1752P]$ where $P=(Fo^2+2Fc^2)/3$

Table 2. Atomic coordinates ($x10^4$) and equivalent isotropic displacement parameters ($Å^2x10^3$) for $AuPb_2I_7$ at 298 K with estimated standard deviations in parentheses.

Label	x	y	z	Occupancy	U_{eq}^*
Au	5000	5000	5000	1	24(1)
Pb	1641(2)	2749(1)	8594(1)	1	37(1)
I1	7315(2)	7904(2)	4043(1)	1	26(1)
I2	4704(2)	6069(2)	6916(1)	1	26(1)
I3	-1961(2)	-349(2)	8621(1)	1	30(1)
I4	5000	5000	0000	1	33(1)

*U_{eq} is defined as one third of the trace of the orthogonalized U_{ij} tensor.

Table 3. Anisotropic displacement parameters ($Å^2x10^3$) for $AuPb_2I_7$ at 298 K with estimated standard deviations in parentheses.

Label	U_{11}	U_{22}	U_{33}	U_{12}	U_{13}	U_{23}
Au	27(1)	29(1)	16(1)	-11(1)	3(1)	-3(1)
Pb	29(1)	40(1)	43(1)	-14(1)	4(1)	-10(1)
I1	36(1)	32(1)	23(1)	-17(1)	3(1)	-2(1)
I2	46(1)	38(1)	20(1)	-20(1)	8(1)	-9(1)
I3	22(1)	30(1)	25(1)	-10(1)	1(1)	-2(1)
I4	24(1)	32(1)	24(1)	-10(1)	0(1)	-9(1)

The anisotropic displacement factor exponent takes the form: $-2\pi^2[h^2a^{*2}U_{11} + ... + 2hka^*b^*U_{12}]$.

Table 4. Selected Bond lengths [Å] and Bond angles [°] for $AuPb_2I_7$ Pb2 at 298 K with estimated standard deviations in parentheses.

Label	Distances	Label	Angles
Au – I1 x 2	2.6330(9)	I1 – Au – I1	180.0
Au – I2 x 2	2.6344(9)	I1 – Au – I2	88.37(3)
Pb – I3	3.1149(10)	I2 – Au – I1	91.63(3)
Pb – I3	3.1644(10)	I2 – Au – I2	180.0
Pb – I2	3.3407(11)	I3 – Pb – I3	92.00(3)
Pb – I1	3.3529(11)	I3 – Pb – I1	76.56(3)
Pb – I4	3.3849(6)	I3 – Pb – I1	76.97(3)
Pb – I3	3.4617(11)	I3 – Pb – I2	90.28(3)
Pb – I4	3.4714(6)	I3 – Pb – I2	143.69(3)
Pb – I2	3.8247(12)	I2 – Pb – I1	68.71(2)
		Pb – I2 – Pb	77.83(2)
		Au – I1 – Pb	99.69(3)
		Au – I2 – Pb	99.97(3)

Symmetry transformations used to generate equivalent atoms:

(1) -x+1,-y+1,-z+1 (2) x+1,y,z (3) x-1,y,z

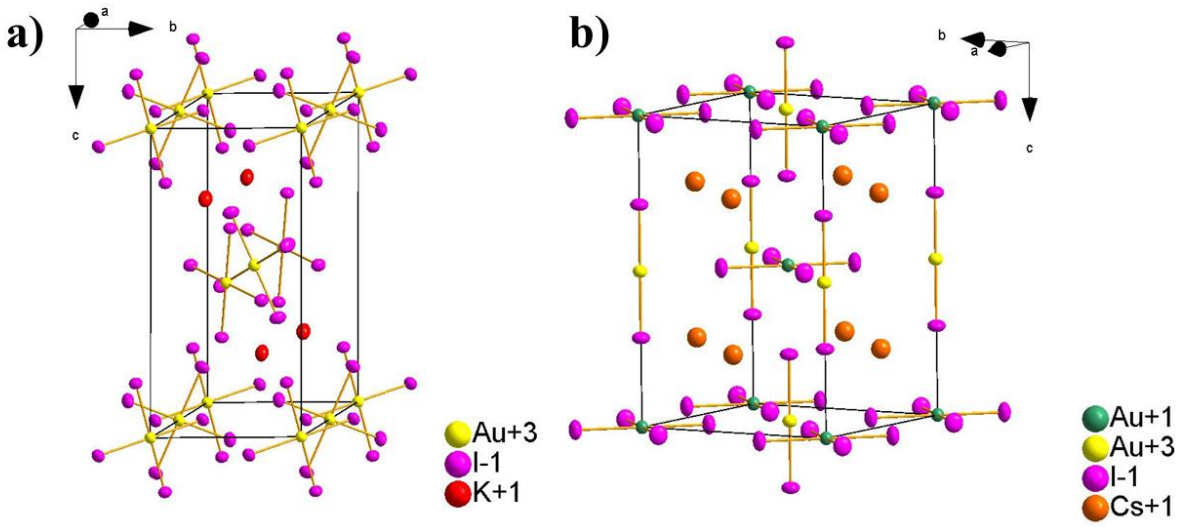

Figure 1. a) The structure of $KAu^{3+}I_4$ where $[AuI_4]^-$ units extend down [010] charge balanced by K^+, a direct analog of $LiAuI_4$ as drawn from reference 16. b) The perovskite-like structure of $Cs_2Au^{1+}Au^{3+}I_6$ where alternating $[AuI_2]^-$ and $[AuI_4]^-$ form pseudo-octahedra around charge balancing Cs cations, as drawn from reference 15. Rb_2 $Au^{1+}Au^{3+}I_6$ forms the same structure.

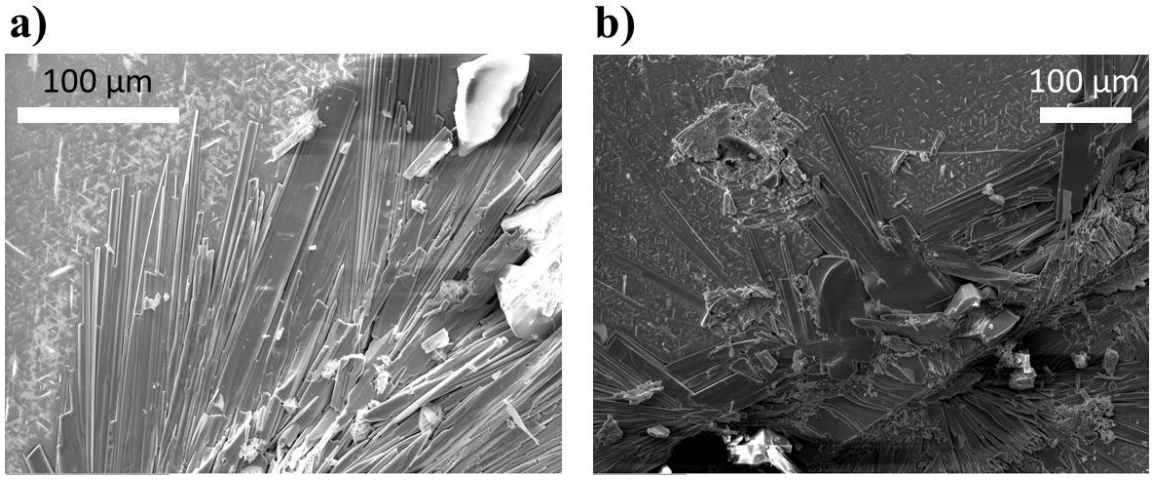

Figure 2. SEM Images of single crystals of $AuPb_2I_7$ growing on the surface of recrystallized PbI_2. Crystals tend to grow near edges where nucleation begins to occur.

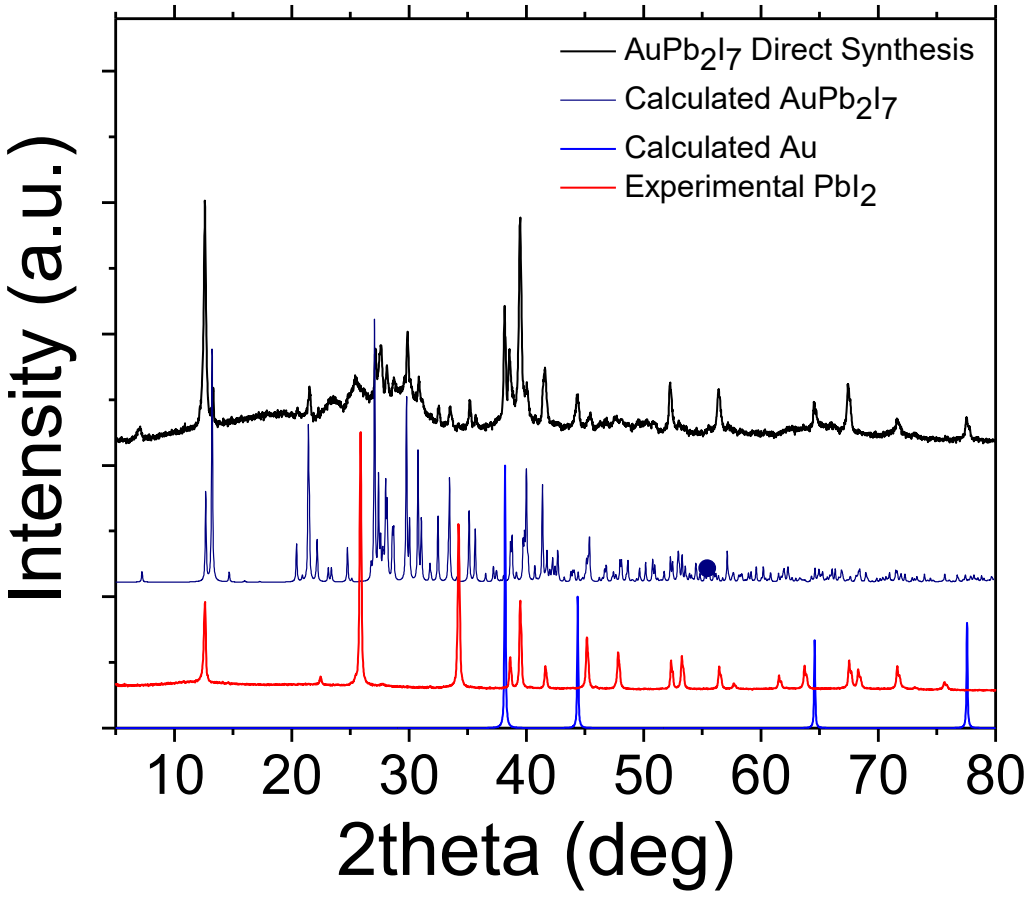

Figure 3. A typical powder diffraction pattern for the reaction mixture of $AuPb_2I_7$. Au and PbI_2 are clearly represented in the pattern, but peaks of the calculated pattern from single crystal data confirms the presence of the title compound.

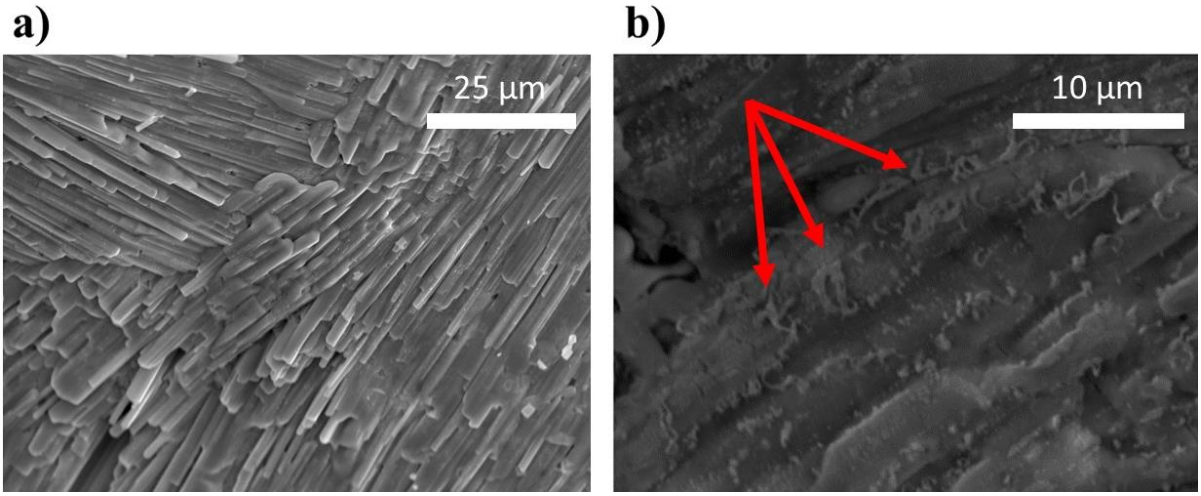

Figure 4. a) A larger forest of needles found after vapor transport. These crystals still grow as layers on top of PbI_2 substrate. b) Au metal expelling from needles of $AuPb_2I_7$ one month after preparation.

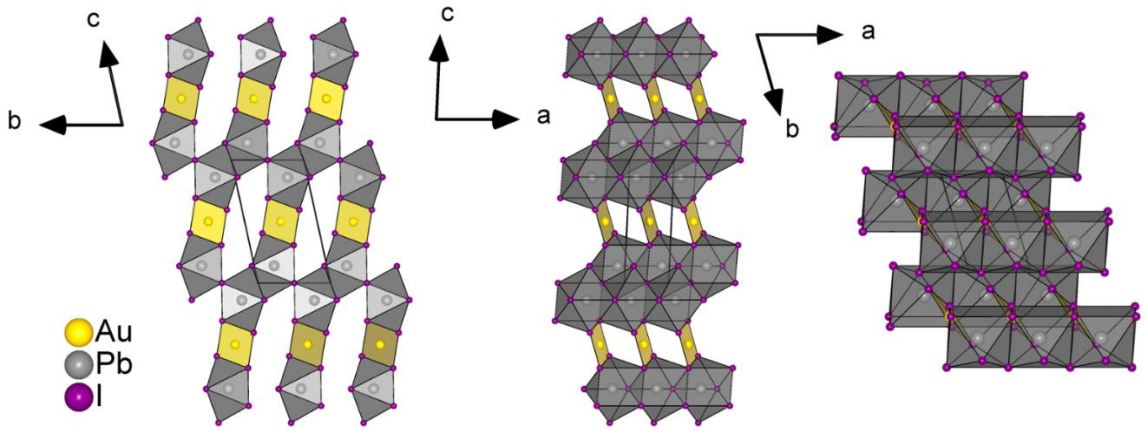

Figure 5. Left) A projection of along [100] of the pseudo-layers in a 3 x 3 x 3 supercell of $AuPb_2I_7$. $^1/_\infty[Pb_2I_2]^{2+}$ can be seen propagating down [100] and bridged by Au^{3+}. Middle) A projection down [010] further demonstrates the pseudo-layered nature of the system. Right) The projection down [001] which shows the corrugated nature of the pseudo-layers.

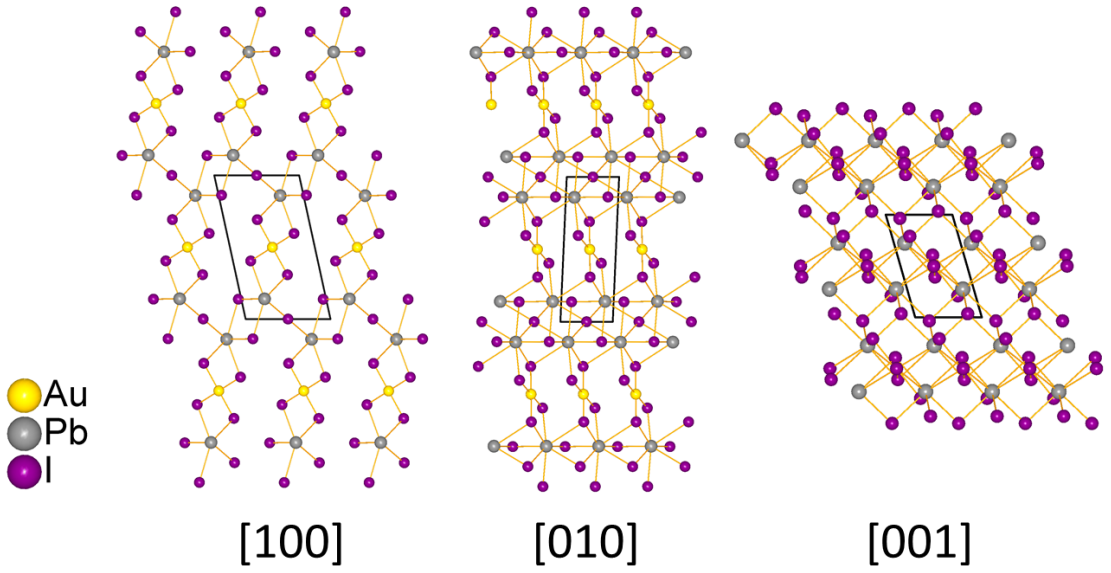

Figure 6. Stick and ball model of the structure of $AuPb_2I_7$ viewed down the three different crystallographic directions. In the view down the [001] direction the Au are totally eclipsed.

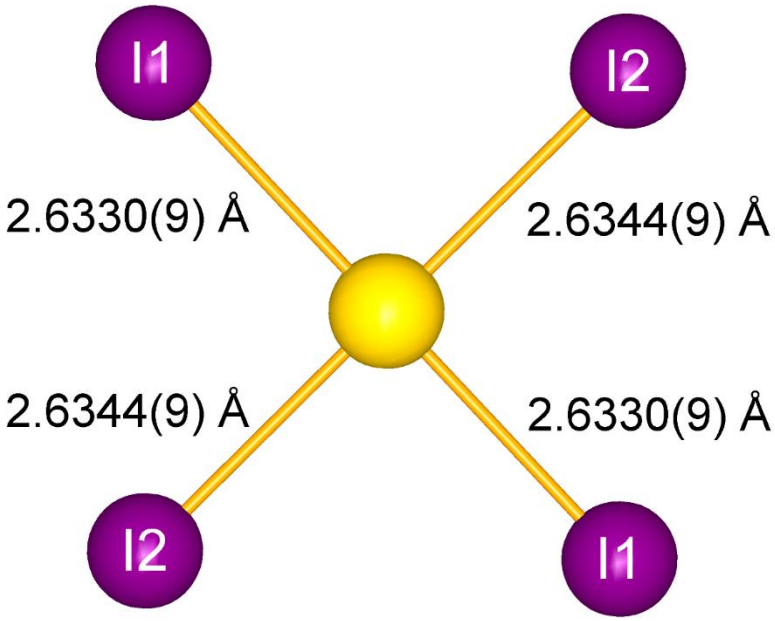

Figure 7. Au^{3+} center in a square planar site of I atoms with bond lengths of 2.6330(9) and 2.6344(9) Å.

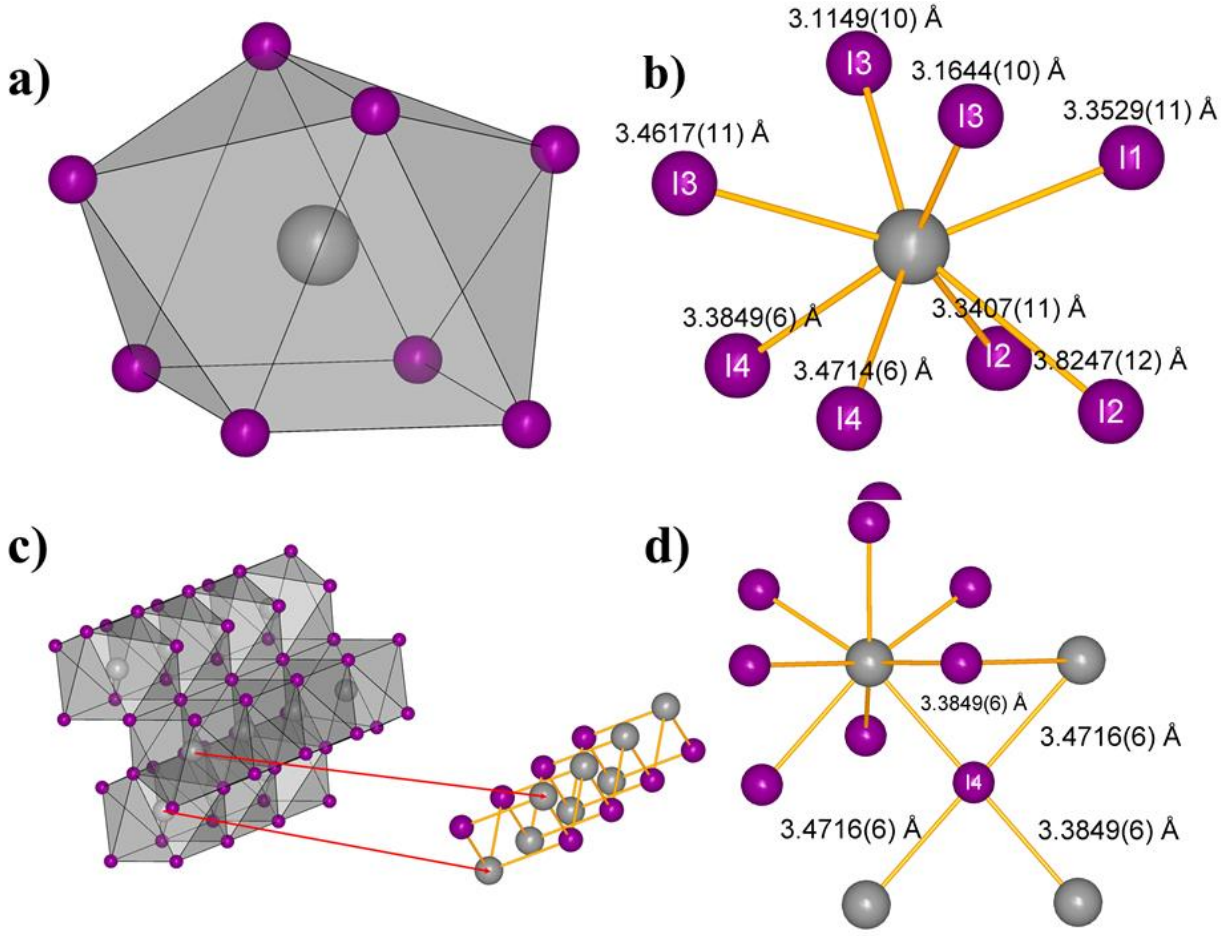

Figure 8. a) The distorted hendecahedron that Pb forms when fully coordinated to neighboring I atoms. b) Atoms labels and bond distances for the Pb hendecahedron in the same relative representation as given in a. c) The greater packing of the Pb polyhedra that extend form the pseudo-layers that are bridged by Au^{3+} with a representation of the $1/\infty[Pb_2I_2]^{2+}$ backbone in the same orientation. d) The square planar orientation of I bridging the $^{1}/_{\infty}[Pb_2I_2]^{2+}$ units to facilitate coordination down [010].

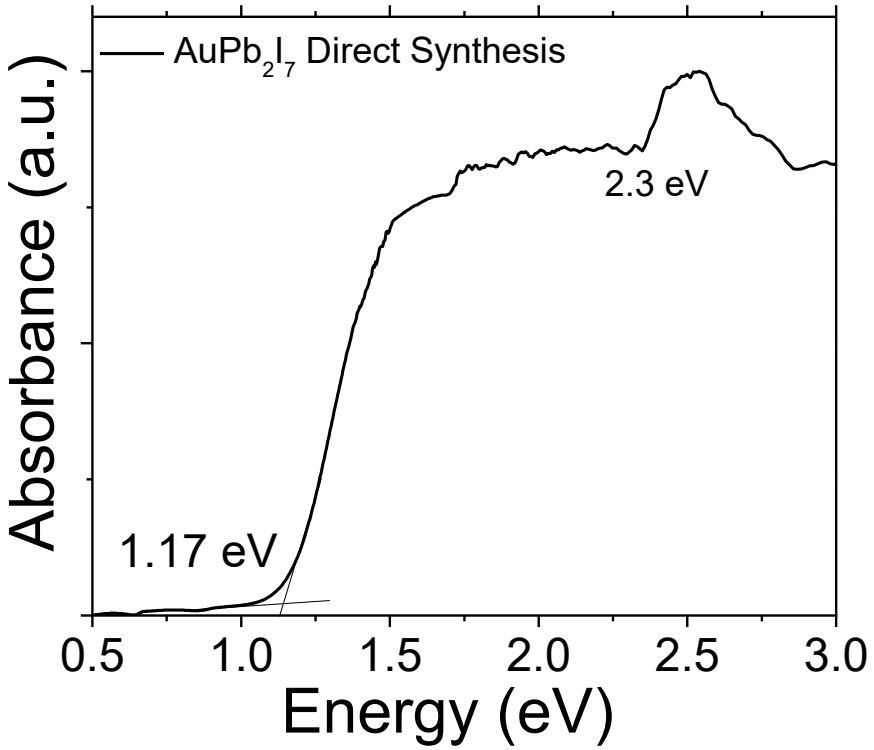

Figure 9. The optical absorbance of a mixture of $AuPb_2I_7$ with some contaminant PbI_2 that can be observed at 2.3 eV. The band gap for the title compound was determined to be 1.17 eV and a direct function of the $[AuI_4]^-$ unit in the structure.

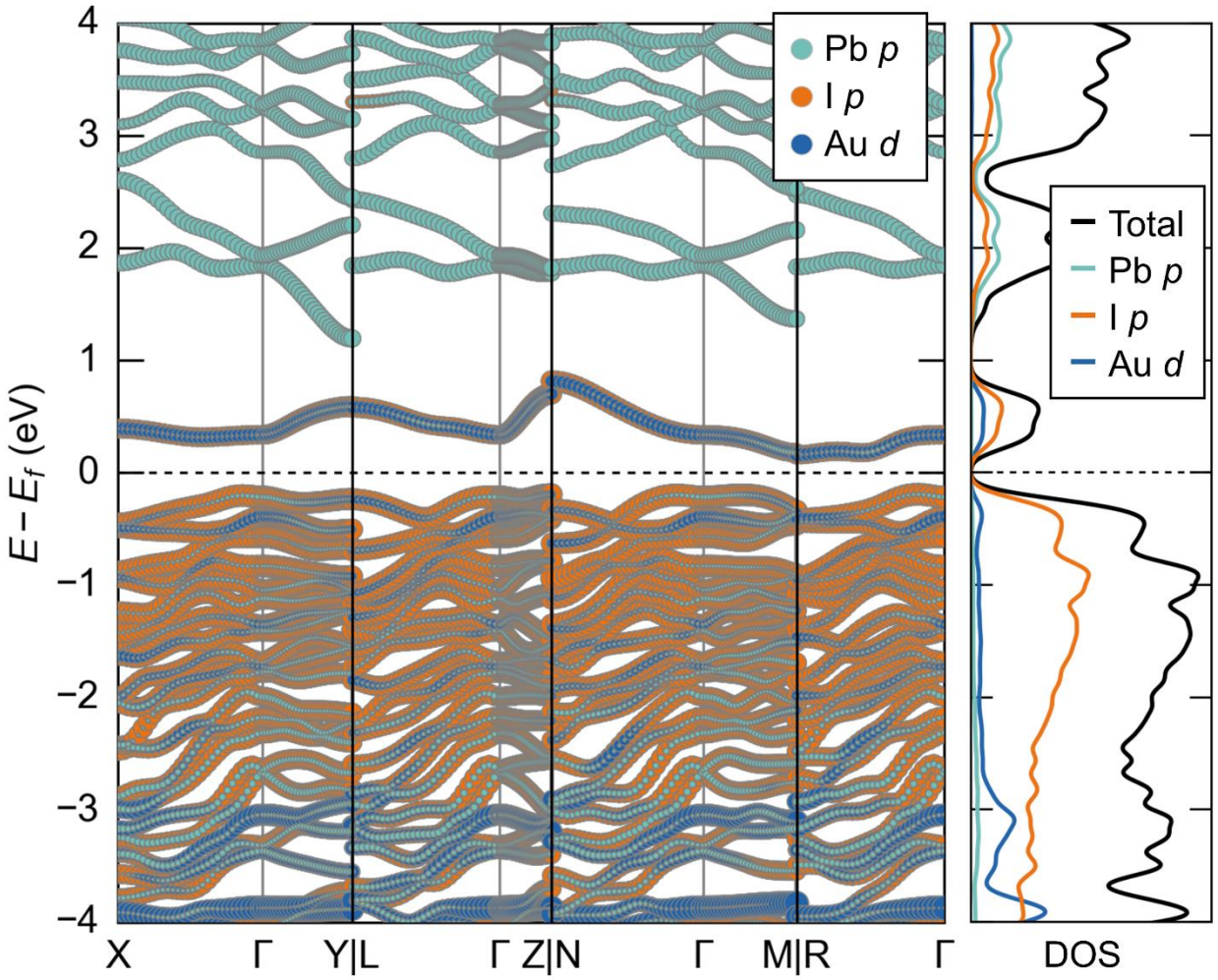

Figure 10. Electronic band structure and density of states (DOS) for $AuPb_2I_7$ from density functional theory, calculated using the generalized gradient approximation (GGA–PBE, with spin-orbit coupling). Orbital projections indicate the bandgap is dominated by filled I *p* states and empty Au *d* states (consistent with the square planar environment for Au^{3+}), while the empty Pb *p* orbitals lie higher in energy.

For Table Of Contents Only

We report unusual Au^{3+} ternary halide $AuPb_2I_7$ has been isolated from reactions of AuI, PbI_2, and I_2 and crystallizes in the triclinic *P*-1 space group as micron-scale needles with cell dimensions *a* = 4.5170(3) Å, *b* = 7.3847(4) Å, *c* = 12.2970(7) Å, α = 76.374(4)°, β = 83.711(4)°, γ = 72.987(3)° at room temperature. Optical absorption characterization and theoretical calculations demonstrate the material is an indirect gap semiconductor.

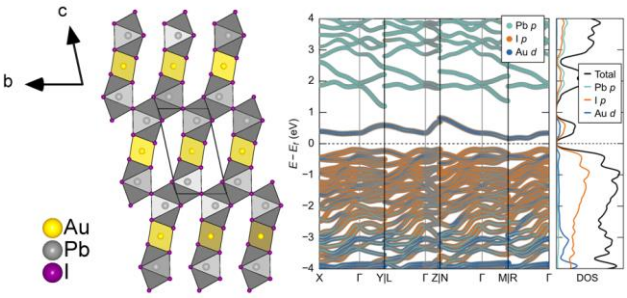

$AuPb_2I_7$: A Narrow Bandgap Au^{3+} Iodide Semiconductor

Grant C. B. Alexander[1], Douglas H. Fabini[2,3], Ram Seshadri[2,3,4], and Mercouri G. Kanatzidis[1,]*

[1] Department of Chemistry, Northwestern University, Evanston, Illinois 60208, United States

[2] Materials Research Laboratory, [3] Materials Department, and [4] Department of Chemistry and Biochemistry, University of California, Santa Barbara, California 93106, USA

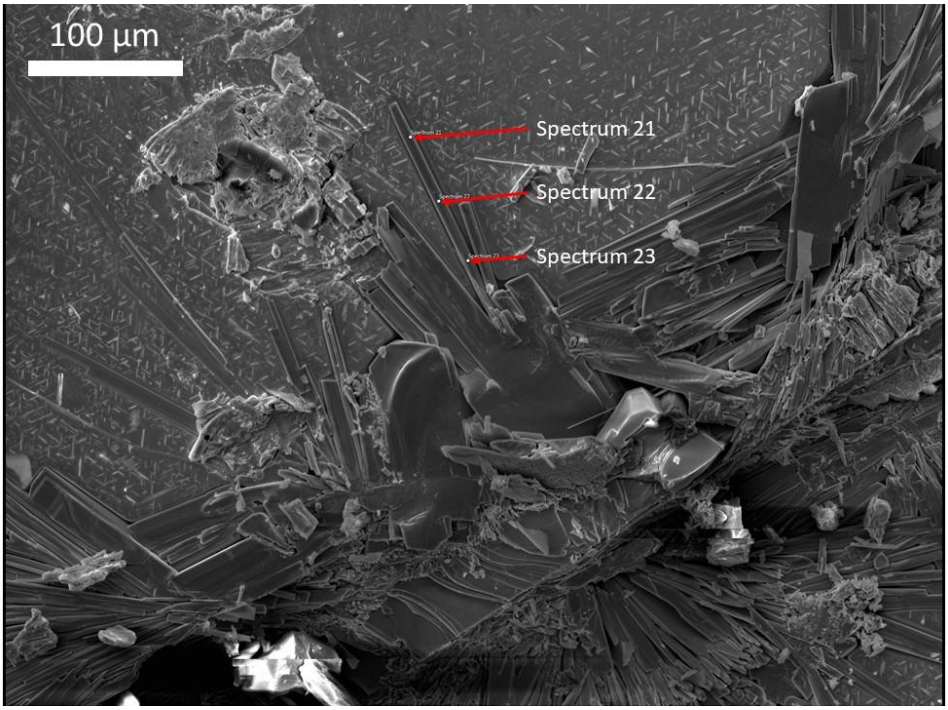

Figure S1. SEM image of the regions chosen to grather EDS data from $AuPb_2I_7$. Due to growth on the surface of PbI_2, often the pentration depth of the electron beam will be greater than the thickness of the crystal resulting in overepresented Pb and I atomic %.

Table S1. SEM-EDS Spectra Results of $AuPb_2I_7$ as assessed from the regions in Figure S1 in Atomic %.

Spectrum Label	Spectrum 21	Spectrum 22	Spectrum 23
I	68.35	67.08	67.84
Au	10.14	10.12	10.35
Pb	21.51	22.79	21.81
Total	100	100	100

Table S2. Average Values and Standard Deviation of SEM-EDS Results from Table S1.

Atom Type	I	Au	Pb
Max	68.4	10.4	22.8
Min	67.1	10.1	21.5
Average	67.8	10.2	22.0
Standard Deviation	0.64	0.12	0.67
Relative Ratio (Based on Au)	6.6	1	2.2

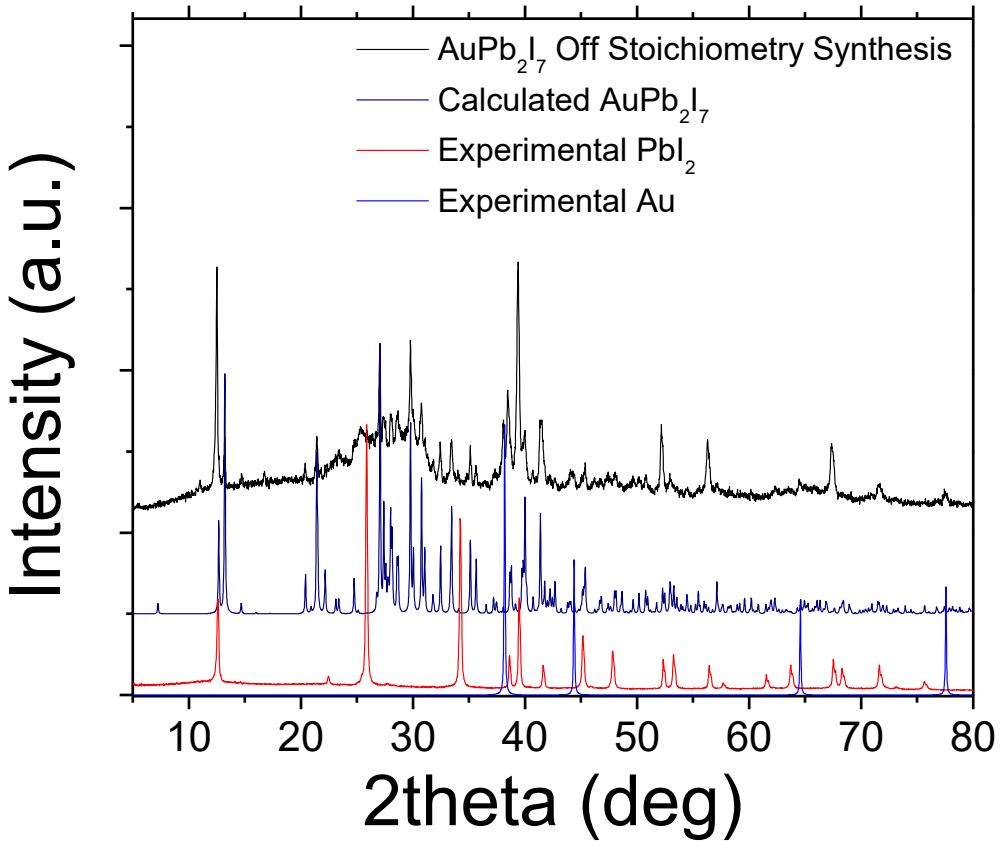

Figure S2. Powder diffraction from off stoichiometric syntheses also shows the presence of the tittle compound despite not having additional iodine to mitigate the disproportionation of Au.

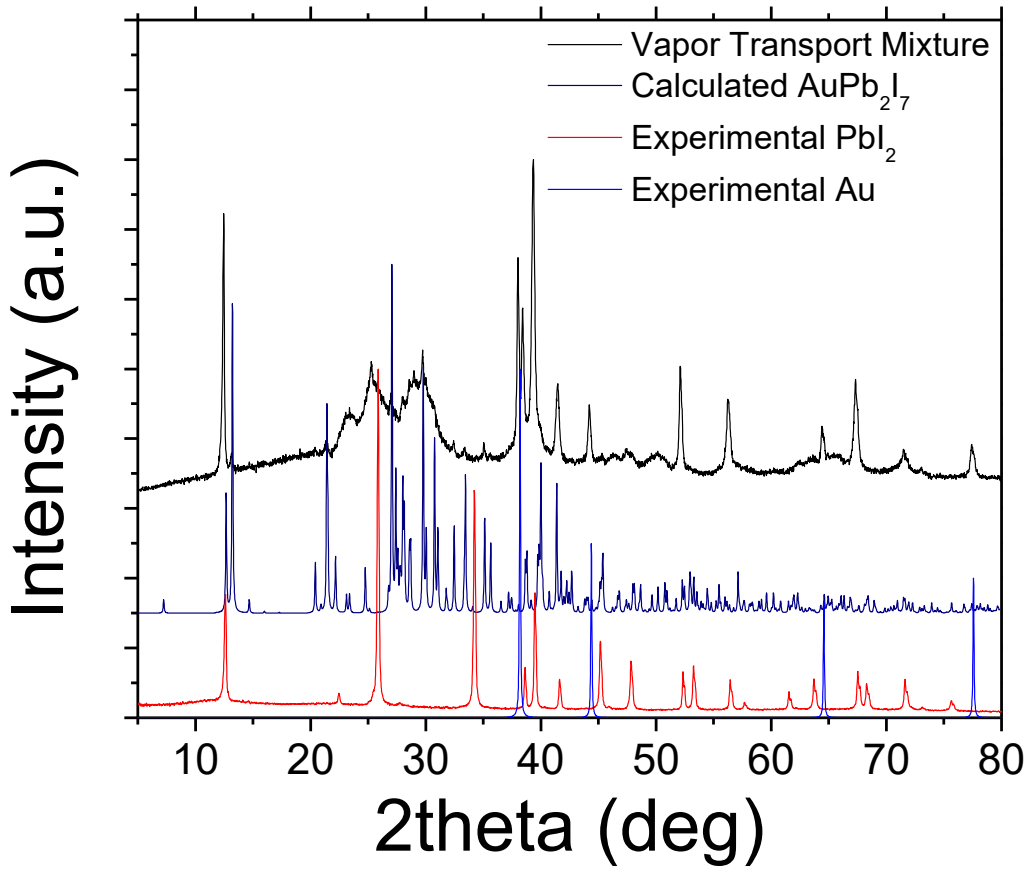

Figure S3. Powder diffraction from the vapor transport mixture shows little evidence of the title compound despite having the most observed by electron microscopy. Due to transport of unreacted PbI_2 away from the melt the mixture that remained in the hot end of the tube was far more gold rich as further described in Figure S4.

Figure S4. Vapor Transport tube after the transport experiment shows the transported PbI_2 on the right side of the image. The black solid on the left hand side is the remaining $AuPb_2I_7$ grown on PbI2, with a dominant amount of metallic gold. This was in the hot zone.

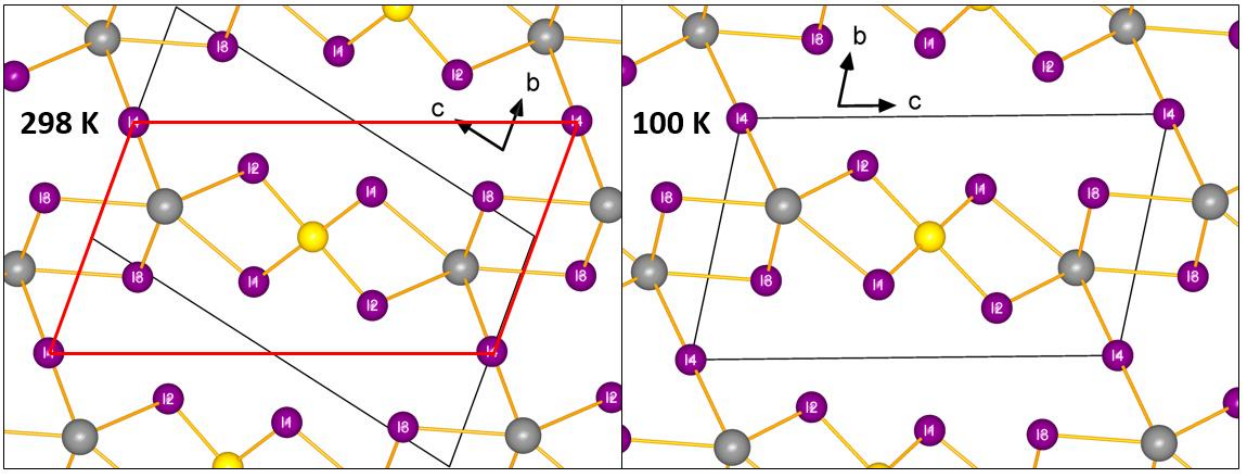

Figure S5. Unit cells of $AuPb_2I_7$ at 298 K and 100 K with the low temperature cell superimposed in red. Due to the change in Au – I bond lengths at low temperature and the general decrease of Pb – I bond distances the I4 – I4 distance decreases and becomes the c axis of the low temperature unit cell.

Table S3. Atomic coordinates ($x10^4$) and equivalent isotropic displacement parameters ($Å^2x10^3$) for $AuPb_2I_7$ at 100 K with estimated standard deviations in parentheses.

Label	x	y	z	Occupancy	U_{eq}*
Au	5000	5000	5000	1	9(1)
Pb	8374(2)	3660(1)	8591(1)	1	13(1)
I4	5000	0	0	1	9(1)
I3	1961(3)	6750(2)	8626(1)	1	10(1)
I1	2668(3)	3038(2)	4039(1)	1	10(1)
I2	5226(3)	2018(2)	6927(1)	1	11(1)

*U_{eq} is defined as one third of the trace of the orthogonalized U_{ij} tensor.

Table S4. Anisotropic displacement parameters ($Å^2x10^3$) for $AuPb_2I_7$ at 100 K with estimated standard deviations in parentheses.

Label	U_{11}	U_{22}	U_{33}	U_{12}	U_{13}	U_{23}
Au	10(1)	12(1)	6(1)	-4(1)	2(1)	-5(1)
Pb	11(1)	14(1)	15(1)	-4(1)	1(1)	-7(1)
I4	9(1)	10(1)	8(1)	-4(1)	2(1)	-4(1)
I3	9(1)	13(1)	9(1)	-4(1)	3(1)	-7(1)
I1	13(1)	13(1)	8(1)	-5(1)	2(1)	-6(1)
I2	15(1)	12(1)	8(1)	-5(1)	0(1)	-4(1)

The anisotropic displacement factor exponent takes the form: $-2\pi^2[h^2a^{*2}U_{11} + ... + 2hka^*b^*U_{12}]$.

Table S5. Selected Bond lengths [Å] for $AuPb_2I_7$ Pb2 at 298 K and 100 K with estimated standard deviations in parentheses.

	298 K	**100 K**
Label	Distances	Distance
Au – I1 x 2	2.6330(9)	2.5464(12)
Au – I2 x 2	2.6344(9)	2.7986(15)
Pb – I3	3.1149(10)	3.1029(17)
Pb – I3	3.1644(10)	3.1493(15)
Pb – I2	3.3407(11)	3.2144(15)
Pb – I1	3.3529(11)	3.5209(18)
Pb – I4	3.3849(6)	3.4794(13)
Pb – I3	3.4617(11)	3.3355(16)
Pb – I4	3.4714(6)	3.6371(17)
Pb – I2	3.8247(12)	3.5658(18)

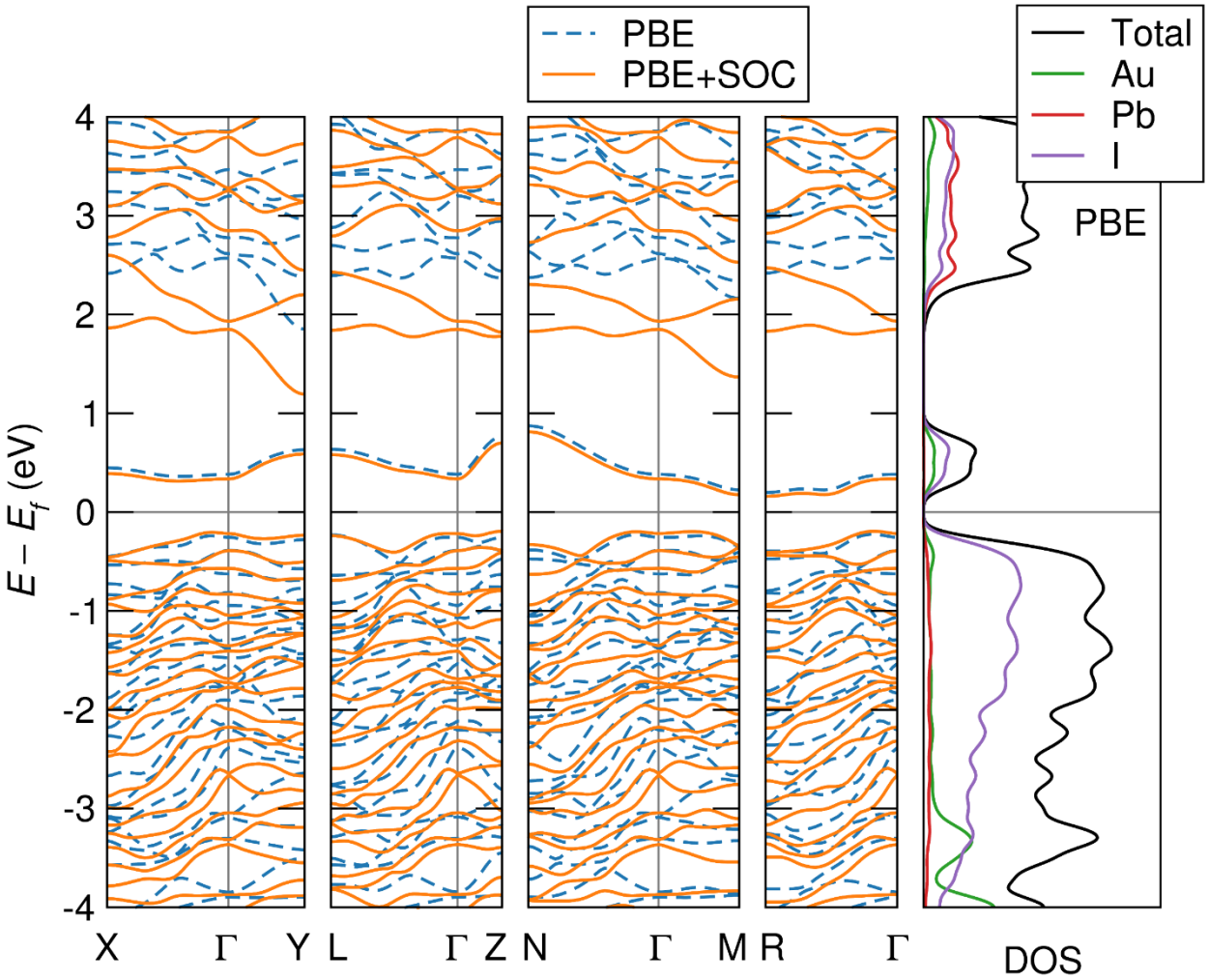

Figure S6. Electronic band structure and density of states (DOS) for $AuPb_2I_7$ from density functional theory, calculated using the generalized gradient approximation (GGA–PBE). The band structure is shown with and without the inclusion of spin-orbit coupling (SOC), which most strongly affects states with Pb character.